



**HAL**  
open science

## Towards large-scale city reconstruction from satellites

Liuyun Duan, Florent Lafarge

► **To cite this version:**

Liuyun Duan, Florent Lafarge. Towards large-scale city reconstruction from satellites. European Conference on Computer Vision (ECCV), Oct 2016, Amsterdam, Netherlands. hal-01352466

**HAL Id: hal-01352466**

**<https://inria.hal.science/hal-01352466>**

Submitted on 8 Aug 2016

**HAL** is a multi-disciplinary open access archive for the deposit and dissemination of scientific research documents, whether they are published or not. The documents may come from teaching and research institutions in France or abroad, or from public or private research centers.

L'archive ouverte pluridisciplinaire **HAL**, est destinée au dépôt et à la diffusion de documents scientifiques de niveau recherche, publiés ou non, émanant des établissements d'enseignement et de recherche français ou étrangers, des laboratoires publics ou privés.

# Towards large-scale city reconstruction from satellites

Liuyun Duan and Florent Lafarge

Inria

firstname.lastname@inria.fr

**Abstract.** Automatic city modeling from satellite imagery is one of the biggest challenges in urban reconstruction. Existing methods produce at best rough and dense Digital Surface Models. Inspired by recent works on semantic 3D reconstruction and region-based stereovision, we propose a method for producing compact, semantic-aware and geometrically accurate 3D city models from stereo pair of satellite images. Our approach relies on two key ingredients. First, geometry and semantics are retrieved simultaneously bringing robustness to occlusions and to low image quality. Second, we operate at the scale of geometric atomic region which allows the shape of urban objects to be well preserved, and a gain in scalability and efficiency. We demonstrate the potential of our algorithm by reconstructing different cities around the world in a few minutes.

**Keywords:** 3D reconstruction, city modeling, satellite imagery, urban scenes

## 1 Introduction

Automatic city modeling has received an increasing interest during the last decade. In applicative fields such as urban planning, telecommunications and disaster control, producing compact and accurate 3D models is crucial. Aerial acquisitions with Lidar scanning or multi-view imagery constitute the best way so far to automatically create 3D models on large-scale urban scenes [1]. Because of high acquisition costs and authorization constraints, aerial acquisitions are, however, restricted to some spotlighted cities in the world. In particular, Geographic Information System (GIS) companies propose catalogs with typically a few hundred cities in the world. Satellite imagery exhibits higher potential with lower costs, a worldwide coverage and a high acquisition frequency. Satellites have however several technical restrictions that prevent GIS practitioners from producing compact city models in an automatic way [2].

Inspired by recent works on semantic 3D reconstruction and region-based stereovision, we propose a method for producing compact, semantic-aware and geometrically accurate 3D city models from stereo pairs of satellite images. Our approach relies on two key ingredients. First, geometry and semantics are retrieved simultaneously bringing robustness to occlusions and to low image quality. Second, contrary to pixel-based methods, we operate at the scale of geometric atomic region: it allows the shape of urban objects to be better preserved, and also a gain in scalability and efficiency. Figure 1 illustrates our goal.

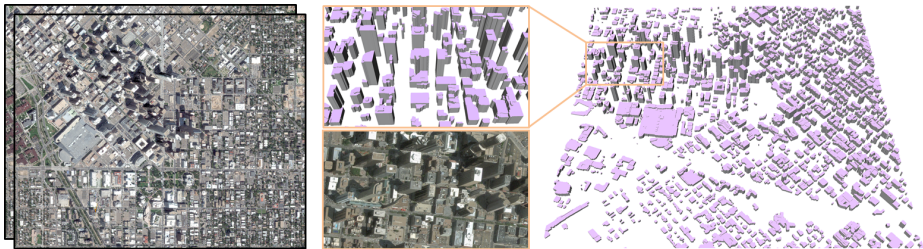


**Fig. 1.** Reconstruction of Denver downtown. Starting from a stereo pair of satellite images (left), our algorithm produces a compact and semantic-aware 3D model (right) in a few minutes.

## 2 Related works

Our review of previous work covers three main facets of our problem: urban reconstruction, region-based stereo matching, and object polygonalization.

*Urban reconstruction.* Reconstruction of urban objects and scenes has been deeply explored in vision, with a quest towards full automation, quality and scalability, and robustness to acquisition constraints [1]. In this field, geometry and semantics are closely related. The most traditional strategy consists in retrieving semantics before geometry. In many city modeling methods [3,4,5], data are first classified so that the subsequent 3D reconstruction can be adapted to the nature of urban objects. Buildings are the most common reconstructed objects, either from multiview imagery [6,7,8] or airborne Lidar [4,9]. Recent works [10,11,12] demonstrate that the simultaneous extraction of geometry and semantics, also known as semantic 3D reconstruction, outclasses multiple step strategies in terms of output quality. However, these works typically suffer from a low scalability and often produce 3D models without structural consideration. Semantic 3D reconstruction remains a challenge at the scale of satellite images.

*Region-based stereo matching.* Numerous works have been proposed in stereo matching [13]. While well-established methods as the Semi-Global Matching (SGM) algorithm [14] reason at the scale of the pixel, some works focus on matching image regions to more accurately preserve object boundaries [15,16]. Beyond boundary accuracy, region-based stereo matching methods can offer high scalability and time-efficiency [17]. Some works [18,19] also combine object segmentation or classification with stereo matching in unified frameworks. Inference for these models is, however, a complex task that requires time-consuming optimization procedures. Overall, most of these methods are not adapted to satellite images whose wide baselines typically produce severe occlusion problems that are not specifically handled. The additional use of geometric primitives as line-segments usually helps to better interpret occluded parts of images [20].

*Object polygonalization.* Capturing objects by polygonal shapes provides a compact and structure-aware representation of the object contours. It is particularly adapted at

representing regular objects as roofs from images. Object polygonalization methods typically depart from the detection of line-segments which are then assembled into polygons. This second step can be done, for instance, by searching for cycles in a graph of line-segments [21], or by connecting line-segments with a gap filling strategy [22]. Grouping atomic regions [23] is also a possible approach, especially when the number of objects is high, and the input image is big. It requires, however, a post-processing step to vectorize chains of pixels into polygons with typically a loss of accuracy.

### 3 Positioning and contributions

Satellite context imposes a set of technical constraints with respect to traditional aerial acquisitions, in particular (i) a lower pixel resolution, typically  $\geq 0.5$  meter, (ii) a lower signal-to-noise-ratio impacting the image quality, and (iii) a wider baseline to guarantee a reasonable depth accuracy. Although these constraints have a low impact on some applications as change detection [24] or generation of dense Digital Surface Models [25], they challenge the automatic reconstruction of compact and semantic-aware city models.

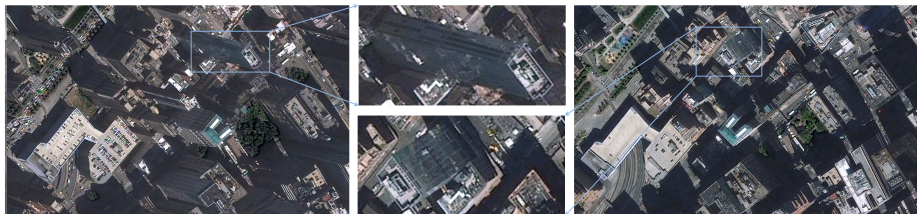


**Fig. 2.** Satellite context. A wide baseline is a necessity to reach reasonable depth accuracy, but brings severe occlusion problems. A facade side is typically visible only in one image (see close-ups). Note also the high proportion of shadow and the time-varying objects as cars.

We propose an automatic city modeling method from satellite imagery whose output approaches the quality of 3D-models delivered by airborne-based methods. We consider as input a calibrated stereo pair of satellite images. Our output city model is a compact mesh composed of ground and building objects. Buildings are represented with a Level Of Detail 1 (LOD1) of the CityGML formalism [26], *ie* piecewise planar buildings with flat roofs and vertical facades. Our method proceeds with three main steps illustrated on Figure 3.

Our main contributions are (i) a full pipeline for producing compact and semantic-aware city models from satellite images, (ii) a time-efficient and scalable approach based on geometric atomic regions, and able to reconstruct big cities in a few minutes, and (iii) a joint classification and reconstruction process that brings robustness to the low quality of input images.

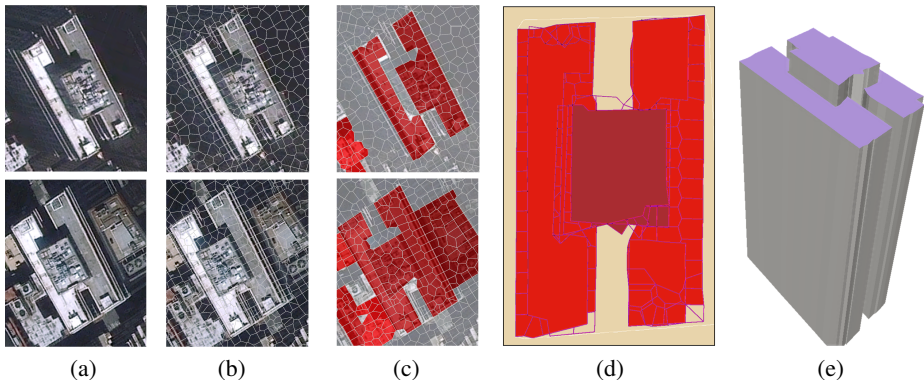


**Fig. 3.** Overview. Input stereo images (a) are first decomposed into atomic convex polygons (b) using existing works (Section 4). In a second step detailed in Section 5, the semantic class and the elevation of each polygon are simultaneously retrieved in the two partitions (c). The last step (Section 6) consists in unifying the two partitions enriched by semantic classes and elevation values into a planimetric elevation representation (d) that allows the generation of the output 3D model (e).

## 4 Polygonal partitioning

Reasoning at the scale of pixel on big satellite images tends to produce non-scalable algorithms that poorly capture geometric information at higher scales [2]. We rather analyze satellite images at the scale of atomic regions, whose efficiency has been demonstrated in shape extraction [23] or stereo matching [17]. Instead of using traditional superpixel methods, we rely on a geometric algorithm that decomposes images into atomic convex polygons [27]. This algorithm is applied independently on both stereo images with a polygon size fixed to 5 pixels (average distance to polygon centroids to its edges) in our experiments. As illustrated on Figure 4, it captures geometric regularities in images by aligning contours of atomic polygons with linear structures as roof edges. Note that the line-segments embedded into the polygonal partitions will be used further in our approach.

The polygons are enriched with an *elevation estimate* which corresponds to the altimetric distance between the observed surface captured in the polygon and the ground. For each polygon, we define its elevation estimate as the difference between the mean of the pixel depths contained inside the polygon (computed by Semi-Global Matching [14] with double checking), and the depth of the ground (computed by a standard Digital Terrain Model (DTM) estimation method [28]). Because of the wide baseline of our stereo pairs, polygons without elevation estimates are frequent, especially when associated to facade elements as illustrated in Figure 4. In return, elevation estimates are relatively accurate and present on a very large majority of roofs. Our strategy is thus to couple these elevation estimates with the geometric information contained in the polygonal partitions to retrieve building contours even for partially occluded roofs.

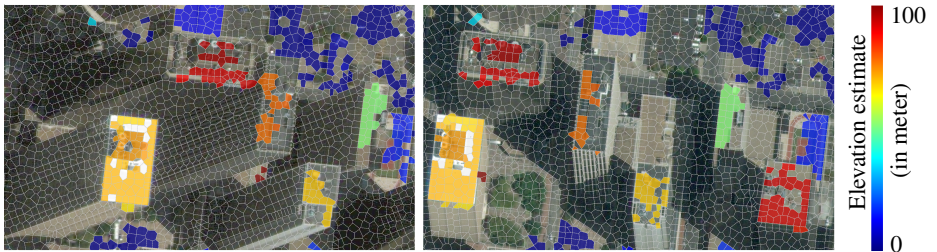


**Fig. 4.** Polygonal partitioning and elevation estimates. Left and right polygonal partitions capture linear structures contained in input images, and in particular building edges. Elevation estimates sparsely cover the polygonal partitions (see colored polygons). Each roof contains at least a few elevation estimates.

We denote by  $\mathcal{P}_l$  and  $\mathcal{P}_r$  the polygonal partitions produced by [27] for the left and the right images respectively.  $\mathcal{P}_l^* \subset \mathcal{P}_l$  represents the set of polygons in  $\mathcal{P}_l$  with elevation estimates. A polygon  $i \in \mathcal{P}_l \cup \mathcal{P}_r$  associated with an elevation estimate  $d_i$  is projected in 3D using the traditional Rational Polynomial Coefficients (RPC) model [29]. Two polygons  $i \in \mathcal{P}_l$  and  $j \in \mathcal{P}_r$  with respective elevation estimates  $d_i$  and  $d_j$  are said to be *imbricate* if the orthographic projections into the horizontal plane of the 3D polygons overlap. In this case, we denote by  $\tau_{ij} \in [0, 1]$  the overlapping ratio of the orthographic projections, ie the intersection area to union area ratio. These notations are illustrated in Figure 5.

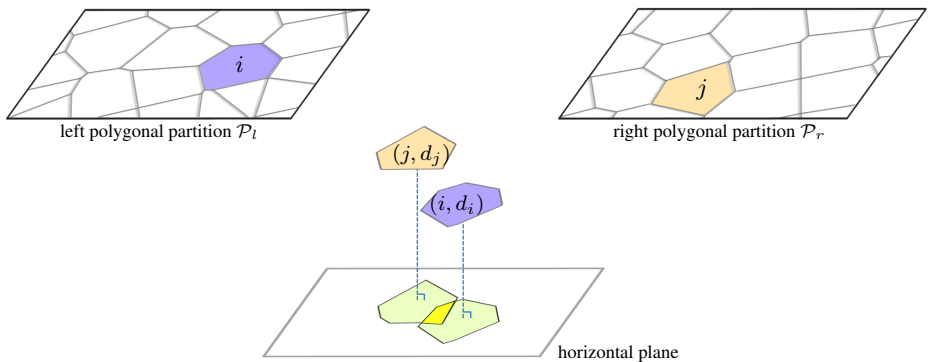


**Fig. 5.** Orthographic projection of polygons. Polygons  $i$  and  $j$  with respective elevation estimates  $d_i$  and  $d_j$  are projected in 3D using the RPC model. These two polygons are imbricate as their orthographic projections into the horizontal plane overlap (see yellow area).

## 5 Joint classification and elevation recovery

Starting from the two polygonal partitions and sparsely distributed elevation estimates, our goal is now to retrieve simultaneously the semantic class and the elevation of each polygon of the partitions.

Two semantic classes of interest are considered: *roof* and *other*. Class *other* mainly refers to ground and facade elements. Because of the wide baseline, most of these elements are only visible in one image. As our main objective is to reconstruct buildings, considering only these two classes is sufficient under the assumption that facades are vertical. Contrary to class *other*, class *roof* is associated with an elevation value. By considering the classification problem as a labeling formulation, the set of possible labels can then be defined as  $L = \{z_1, \dots, z_n, other\}$  where  $z_1, \dots, z_n$  are the  $n$  possible elevation values of a roof. To set  $z_1, \dots, z_n$ , we cluster the set of elevation estimates by Kmeans with  $K = n + 1$ , and associate the  $n$  highest centroids to them. As the ground falls into the class *other*, the centroid with the lowest value is reset to zero. We denote by  $\sigma(z_k)$  the standard deviation of the  $k^{th}$  cluster.

The quality of a configuration of labels  $l \in L^{card(\mathcal{P})}$  is measured through an energy  $U$  of the form:

$$U(l) = \sum_{i \in \mathcal{P}} D_{data}(l_i) + \beta_1 \sum_{(i,j) \in \mathcal{E}_s} V_{smoothness}(l_i, l_j) + \beta_2 \sum_{(i,j) \in \mathcal{E}_c} V_{coupling}(l_i, l_j) \quad (1)$$

where  $D_{data}$  is the unary data term, and  $V_{smoothness}$  and  $V_{coupling}$  are pairwise potentials favoring respectively label smoothness and label coherence between left and right partitions.  $\mathcal{E}_s$  and  $\mathcal{E}_c$  correspond to two sets of pairs of adjacent polygons.  $\beta_1$  and  $\beta_2$  are parameters weighting the three terms of the energy.

*Polygon adjacency.* The two adjacency sets  $\mathcal{E}_s$  and  $\mathcal{E}_c$  impose spatial dependencies between polygons, either within the same polygonal partition for the former or in between the polygonal partitions for the later, as illustrated on Figure 6.

$\mathcal{E}_s$  contains pairs of polygons who share a common edge which is not supported by one of the line-segments embedded into the polygonal partitions. As illustrated in Figure 6-right, this condition on line-segments is particularly efficient for stopping label propagation when meeting building edges.

$\mathcal{E}_c$  is defined as the set of imbricate polygons, ie the pairs of polygons  $i \in \mathcal{P}_l^*$  and  $j \in \mathcal{P}_r^*$  so that  $\tau_{ij} > 0$ .

*Data term.* It measures the coherence between the elevation estimate of a polygon and its proposed label. For polygons without an elevation estimate, we favor the occurrence of the label *other* as a polygon without a depth estimate is most likely to capture an element visible only in one image such as facade and, to a lesser extent, ground. The data term is expressed as

$$D_{data}(l_i) = \begin{cases} 1 - e^{-\frac{(l_i - d_i)^2}{2\sigma(l_i)^2}} & \text{if } i \in \mathcal{P}^* \\ \alpha \cdot \mathbf{1}_{\{l_i \neq other\}} & \text{otherwise} \end{cases} \quad (2)$$

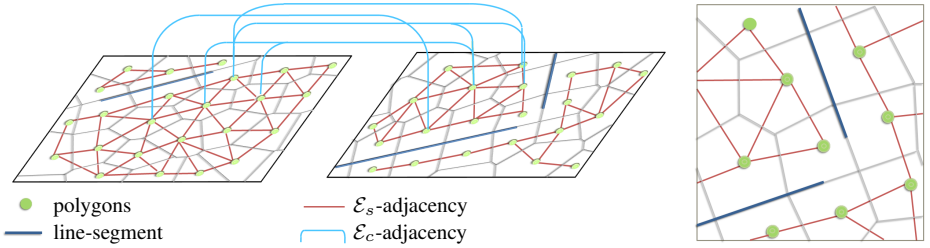


**Fig. 6.** Polygon adjacency. Two types of pairwise interactions between polygons are taken into account in the labeling formulation: within the same partition and in between partitions (left). Line-segments embedded into the partitions prevent neighboring polygons from interacting (right).

where  $d_i$  is the depth estimate of polygon  $i$ ,  $\mathbb{1}_{\{\cdot\}}$  is the characteristic function, and  $\alpha$  is the penalty weight for not choosing *other*. When label *other* is attributed to polygon  $i \in \mathcal{P}^*$ , we set  $l_i$  to 0.

*Smoothness.* The smoothness term penalizes  $\mathcal{E}_s$ -adjacent polygons with different labels using a generalized Potts model:

$$V_{smoothness}(l_i, l_j) = w_{ij} \cdot \mathbb{1}_{\{l_i \neq l_j\}} \quad (3)$$

where the weight  $w_{ij}$  reduces the penalty of having different labels when the radiometry of pixels inside the two polygons is not similar. In practice,  $w_{ij}$  is chosen as one minus the normalized histogram distance in norm  $L_2$ .

*Coupling.* Similarly to the smoothness potential, the coupling term is defined by a generalized Potts model, here, between imbricate polygons.

$$V_{coupling}(l_i, l_j) = \tau_{ij} \cdot \mathbb{1}_{\{l_i \neq l_j\}} \quad (4)$$

where  $\tau_{ij}$  allows polygons with different labels to be penalized proportionally to their overlapping ratio.

*Optimization.* An approximation of the global minimum of the energy is found using the  $\alpha$ - $\beta$  swap algorithm [30]. Figure 7 shows the impact of the different terms of the energy. In the sequel, we call *enriched* partition, a polygonal partition whose polygons have received a class and eventually an elevation value by this energy minimization.

## 6 Fusion of enriched partitions

The projection in 3D of left and right enriched partitions gives two different interpretations of the shape of objects as (i) some roof parts are frequently occluded between the two images, (ii) the shapes of polygons between left and right partitions do not necessarily correspond, and (iii) the coupling term of Eq. 1 is a soft constraint that does not guarantee that imbricate polygons have the same elevation. To unify the two interpretations into a unique 3D model, we project all 3D polygons into the horizontal plane, and relabel elevations inside the new induced horizontal partition.



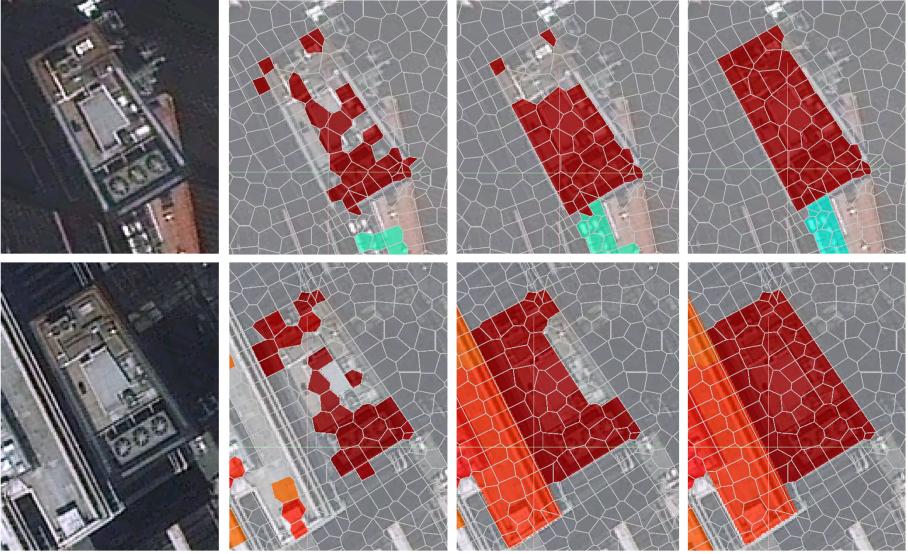


**Fig. 7.** Impact of the different energy terms. Roofs are sparsely labeled using the data term only ( $\beta_1 = \beta_2 = 0$ ,  $2^{nd}$  column). Adding the smoothness potential propagates roof labels while preserving building edges ( $\beta_2 = 0$ ,  $3^{rd}$  column). The labeling coherence between the left and right partitions is enforced considering the complete energy formulation (right column).

*Orthographic projection.* Each polygon  $i \in \mathcal{P}$  whose class is not *other* is projected into the horizontal plane. The superposition of projected polygons from left and right partitions produces a decomposition of the horizontal plane into new polygons that we call *cells*. Note that the cells are not necessarily convex. We denote by  $\mathcal{C}$  the set of cells. Each cell inherits the elevations of the polygons that overlap with it. We denote by  $Z_k$ , the set of elevations inherited by cell  $i \in \mathcal{C}$ . Different types of cells can be distinguished:

- **Coherent cells** are cells that inherit two identical elevations, one from the left partition and one from the right. The elevation value of these cells is not modified further.
- **Conflict cells** are cells that inherit at least one elevation, and that are not coherent cells.
- **Empty cells** are cells without inherited elevation. These cells, which typically fill in the holes in the cell decomposition, mainly corresponds to ground or small roof parts.

We denote by  $\mathcal{C}_{coherent}$ ,  $\mathcal{C}_{conflict}$  and  $\mathcal{C}_{empty}$  these three sets of cells respectively, illustrated in Figure 8.

*Cell relabeling.* For fusing enriched partitions, each conflict or empty cell must be associated with a unique elevation. We relabel those cells using an energy formulation

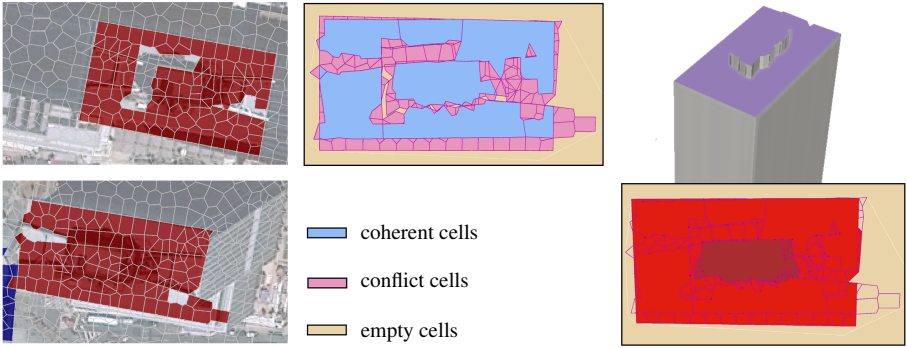


**Fig. 8.** Fusion of enriched partitions. Projecting the enriched partitions (left) into the horizontal plane produces a cell decomposition in which three groups of cells can be distinguished (middle). The relabeling of the elevation of conflict and empty cells gives a unified 3D model (right).

with a standard form:

$$E(x) = \sum_{k \in \mathcal{C}^*} A_k \cdot E_d(x_k) + \lambda \sum_{(k, k') \in \mathcal{N}} L_{kk'} \cdot E_r(x_k, x_{k'}) \quad (5)$$

where  $\mathcal{C}^* = \mathcal{C}_{conflict} \cup \mathcal{C}_{empty}$ , the label  $x_k$  of cell  $k$  is an elevation value in  $Z = \{0, z_1, \dots, z_n\}$ , and  $\mathcal{N}$  is the set of pairs of adjacent cells in  $\mathcal{C}$  that have at least one cell belonging to  $\mathcal{C}^*$ .  $E_d$ ,  $E_r$  and  $\lambda$  are respectively the unary data term, the pairwise potential and the weighting parameter between the two terms.  $A_k$  and  $L_{kk'}$  are respectively the area of cell  $k$ , and the length of the common edge between cells  $k$  and  $k'$ : they are introduced to normalize the energy with respect to the size of cells.

The intuition behind the data term is that (i) an empty cell is more likely to be ground with an elevation value of 0, and (ii) a conflict cell is more likely to be roof with an elevation value as close as possible to its inherited elevations:

$$E_d(x_k) = \begin{cases} 0 & \text{if } k \in \mathcal{C}_{empty} \text{ and } x_k = 0 \\ \min\{|x_k - z|_{z \in Z_k}\} & \text{else if } k \in \mathcal{C}_{conflict} \text{ and } x_k \neq 0 \\ \gamma & \text{otherwise} \end{cases} \quad (6)$$

where  $\gamma$  is a penalty for not respecting this intuition.

The pairwise potential is a generalized Potts model that increases the penalty between two cells when their common edges projected in 3D back-project well into the images. As we consider the pairs of cells with different elevations  $x_k$  and  $x_{k'}$ , each pair has exactly two common edges in 3D: one at elevation  $x_k$ , the other at elevation  $x_{k'}$ . The pairwise term is expressed by

$$E_r(x_k, x_{k'}) = \min(G^l(x_k) + G^l(x_{k'}), G^r(x_k) + G^r(x_{k'})) \cdot \mathbb{1}_{\{x_k \neq x_{k'}\}} \quad (7)$$

where  $G^l(x_k)$  (respectively  $G^r(x_k)$ ) is a back-projection measure of the common edge at elevation  $x_k$  into the left (resp. right) image. In practice, the back-projection measure is defined as the absolute value of one minus the scalar product between the image gradients and the gradients of the back-projected edge.

*Optimization.* For efficiency reasons, the energy minimization is spatially decomposed into independent subproblems. We regroup the connected conflict and coherent cells into clusters while allowing empty cells to be inside. Each cluster intuitively corresponds to a building or a building block. The  $\alpha$ - $\beta$  swap algorithm [30] is then operated over the set of conflict and empty cells of each cluster. Note that, for each cluster, we restrict the label set  $Z$  to the inherited elevations of its cells. Optionally, the optimization can be performed in parallel on each cluster.

*Compact city model.* The ground is represented in 3D by a mesh surface triangulated from the altitude estimates [28]. From the optimal label configuration, roofs are inserted by simply elevated cells to their elevation label from the ground. The facade components are finally added by creating vertical facets between the adjacent cells with different labels.

## 7 Experiments

We experimented our method with stereo pairs from QuickBird2, WorldView2 and Pleiades satellite images with pixel resolution at 0.6, 0.5 and 0.5 meter respectively. All the experiments have been done on a single computer with Intel Core i7 processor clocked at 2GHz.

*Implementation details.* Our algorithm is implemented in C++ using the Computational Geometry Algorithms Library (CGAL) [31] for manipulating geometric data structures in 2D and 3D, and the Geospatial Data Abstraction Library (GDAL) [32] for processing basic operations with satellite images. The cell decomposition in Section 6 is computed using a constrained Delaunay triangulation whose constrained edges correspond to the orthographic projection into the horizontal plane of the polygon edges of both partitions. The number of parameters is large, *ie* 6, but this is the price to pay for a full pipeline combining semantic and geometric considerations in an unsupervised manner. In all our experiments except Fig. 7, we fixed the weights of the two energies to  $\beta_1 = 0.2$ ,  $\beta_2 = 10$  and  $\lambda = 2.5$ , and the penalties to  $\alpha = 0.05$  and  $\gamma = 2$ . The number of possible roof elevations is set to  $n = 50$ , except for US cities where skyscrapers requires increasing its value to 100.

*Robustness.* Our output models provide a faithful LOD1 representation of buildings, as illustrated in Figure 9. With the current satellite resolutions, a more detailed building representation such as LOD2 is not realistic. Cases that challenge our algorithm are the small buildings, typically houses in residential areas, and the textureless and reflective objects which, generally speaking, constitute an important challenge in stereovision. Our method can handle buildings with some parts are visible only in one image. However, large occluded parts can generally not be recovered.

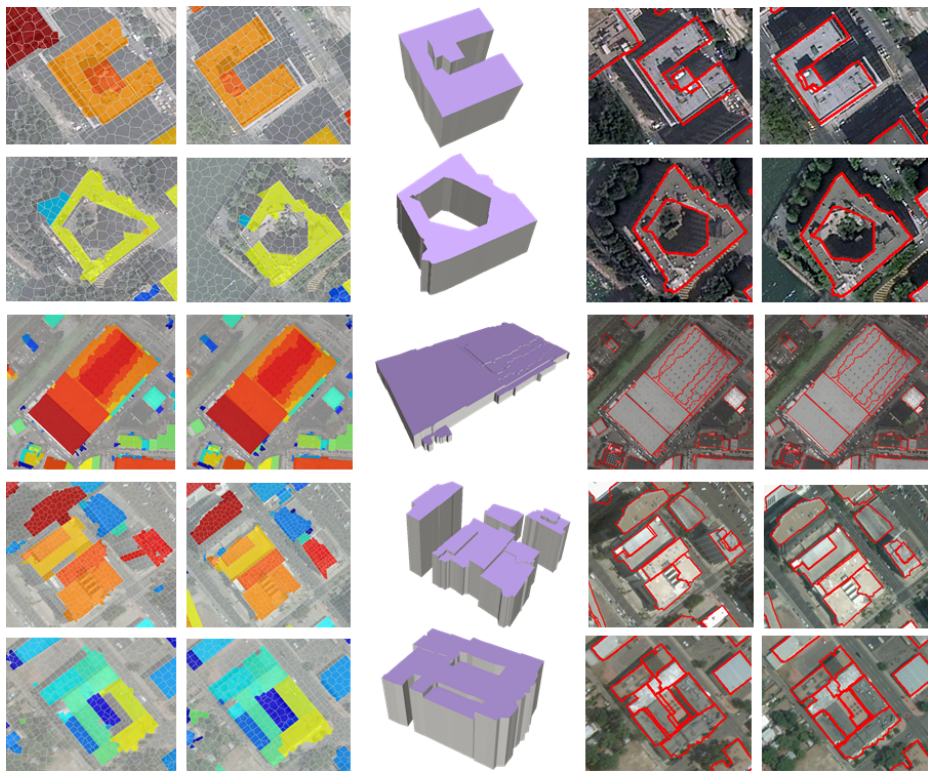


**Fig. 9.** Reconstruction of buildings. On simple buildings (top examples), left and right enriched partitions (left columns) are relatively similar. For more complex buildings (bottom examples), enriched partitions are more different: their fusion allows us to find a consensual 3D output model. With freeform architectural structures (middle example), curved roofs are roughly approximated by a step-like geometry. The back-projection into the input images of the roof edges from the output 3D model shows a good accuracy of both building elevations and contours (see red lines in right columns).

*Scalability.* Our algorithm has been tested on several cities presenting different urban landscapes, as shown on Figures 3 and 10. Dense downtowns in antique cities such as Alexandria, Egypt, are particularly challenging with narrow streets and small buildings massively connected. Our algorithm sometimes fails separating blocks in between these narrow streets as their width can be smaller than the size of our polygons. Business districts of US cities as Denver or New York is the opposite landscape: buildings are large, tall and fairly separated from each other. Our algorithm typically performs better on such areas. In terms of classification, buildings are globally well detected. One of the main reasons is because we do not rely on a radiometric description of buildings. At the scale of big cities, the radiometric variability of buildings is too high to draw likelihoods. Buildings can be missed when there are not enough elevation estimates. This situation is relatively marginal in practice: a visual comparison between our output



**Fig. 10.** Reconstruction of cities. Our algorithm performs on different types of urban landscapes, including dense downtown (top left), antique city (bottom left), and US downtown (bottom right). Each model was obtained from one stereo pair of satellite images.

3D model of Denver and the building footprints of a cadastral map give us less than 5% of missed buildings and 14% of invalid buildings, ie buildings with at least 20% of their footprints missed or over-detected.

*Performance.* Timings and complexity of output 3D models are given for different cities in Table 1. Input satellite images have typically around 30Mpixels. Each of the three steps of our method takes a few minutes from a typical stereo pair of satellite images. For very dense cities, fusion is the most time-consuming step as the high density of buildings generates complex cell decompositions. For cities with more space in between the buildings such as New York or Denver, fusion is quite fast. Running times for joint classification and elevation recovery, and polygonal partitioning do not depend on the urban landscape, but on the input image size. Overall, the use of compact and efficient geometric data structures allow us to have very competitive timings with respect to airborne-based methods.

	New York City, US	Denvers, US	Seoul, South Korea	Alexandria, Egypt
Polygonal partitioning	0.5 min	1.0 min	0.8 min	0.5 min
Joint classification	2.8 min	4.7 min	3.4 min	2.5 min
Fusion	1.5 min	2.8 min	13.7 min	29.2 min
Total time	4.8 min	8.5 min	17.9 min	32.2 min
Output complexity	0.23M	0.35M	0.89M	1.35M

**Table 1.** Running times and output complexity. The output complexity refers to the number of triangular facets in the output 3D model. Note that the fusion step has been optimized sequentially on each building cluster.

*Comparisons.* While there is no automatic algorithm producing compact and semantic-aware city models from satellite images, we compared our output models to traditional Digital Surface Models generated from stereo matching, following by structure recovery algorithms. As shown in Figure 11, our output model better preserves the building structure while being semantic-aware and compact. We also measure in Figure 12 the geometric accuracy of our method, and compares it with accuracy of an airborne Lidar based algorithm. Although our output is less accurate, the gap is relatively low given the contrast of data accuracy between airborne Lidar and satellite imagery.

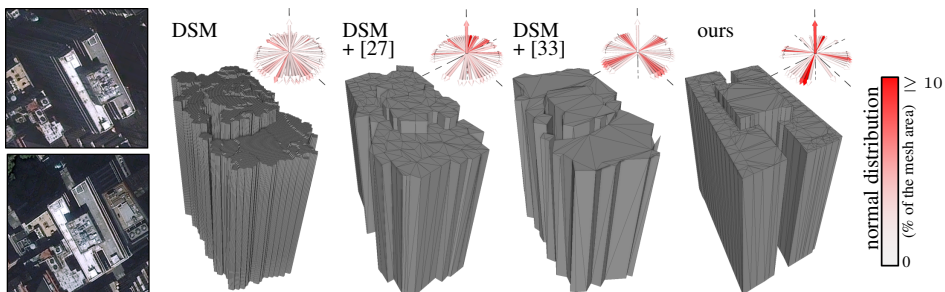


**Fig. 11.** Comparisons with Digital Surface Models. Traditional DSM derived from stereo matching [14] at the pixel scale gives dense and structure-free 3D models. By postprocessing a DSM with Voronoi clustering [27] or with structure-aware mesh simplification [33], we obtain more compact meshes, but the building structure cannot be not restored. Our output model is both compact and structure-aware (see the low number of principal directions in the distribution of output normals).

*Limitations.* Our algorithm has several limitations. First, our output 3D models only contain three semantic labels (ground, roof and facade). The design of our algorithm is, however, flexible enough to account for new urban classes in future works. Second, the limited quality of satellite images makes difficult the reconstruction of small buildings, typically houses in residential areas. Third, our system is robust to occlusions of

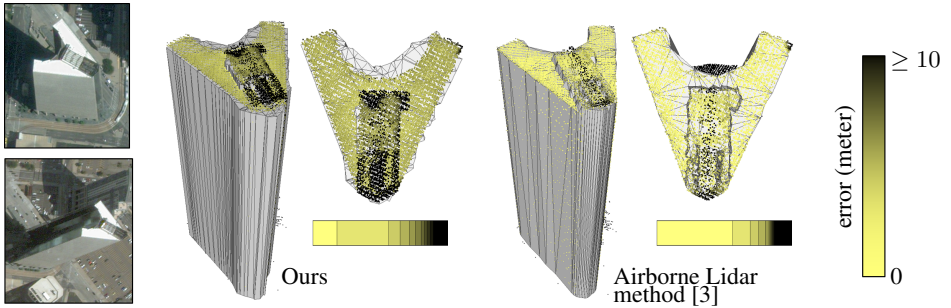


**Fig. 12.** Geometric accuracy. Airborne Lidar scans constitute precise measurements that can be used as Ground Truth to evaluate the geometric accuracy of our outputs (see the distribution of errors on the horizontal histogram). While a state-of-the-art airborne Lidar method [3] produces more accurate results with a lower mean error to Lidar points ( $0.9m$  vs  $1.7m$ ), the gap is relatively low given the difference of quality between the two types of inputs.

facades, ground and piece of roofs, but cannot handle severe roof occlusions where a roof is only visible in one image. Our LOD1 representation is also less accurate with freeform architectural roofs as domes or peaky structures. In such cases, roofs are approximated by a step-like geometry whose accuracy depends on the amount of elevation estimates.

## 8 Conclusion

We proposed a full pipeline for producing compact and semantic-aware city models from satellite images. Big cities such as Denver are reconstructed in a few minutes. Our method relies on two key ingredients. First, we reason at the scale of atomic polygons to capture geometry of urban structures while insuring a fast and scalable process. Second, semantics and 3D geometry are retrieved simultaneously to be robust to low resolution and occlusion problems of satellite images. Whereas the quality of our output models is not as accurate as airborne Lidar solutions, our solution outclasses traditional DSM representations, and offers new perspectives in city modeling.

As future work we wish to include more semantic classes into the pipeline, in particular roads and high vegetation. We also would like to investigate the use of geometric regularities at the scale of a district or an entire city as a way to consolidate input data and reinforce the structure-awareness of the models of buildings.

## Acknowledgments

This work was supported by Luxcarta. The authors thank Qian-Yi Zhou, Lionel Laureore, Justin Hyland, Véronique Poujade and Frédéric Trastour for datasets and technical discussions.

## References

1. Musialski, P., Wonka, P., Aliaga, D., Wimmer, M., Van Gool, L., Purgathofer, W.: A survey of urban reconstruction. *Computer Graphics Forum* **32**(6) (2013)
2. Poli, D., Caravaggi, I.: 3d modeling of large urban areas with stereo VHR satellite imagery: lessons learned. *Natural Hazards* **68**(1) (2013)
3. Lafarge, F., Mallet, C.: Building large urban environments from unstructured point data. In: *ICCV*. (2011)
4. Poullis, C., You, S.: Automatic reconstruction of cities from remote sensor data. In: *CVPR*. (2009)
5. Zhou, Q., Neumann, U.: A streaming framework for seamless building reconstruction from large-scale aerial lidar data. In: *CVPR*. (2009)
6. Zebedin, L., Bauer, J., Karner, K., Bischof, H.: Fusion of feature- and area-based information for urban buildings modeling from aerial imagery. In: *ECCV*. (2008)
7. Vanegas, C., Aliaga, D., Benes, B.: Building reconstruction using Manhattan-world grammars. In: *CVPR*. (2010)
8. Verdie, Y., Lafarge, F., Alliez, P.: LOD generation for urban scenes. *ACM Transactions on Graphics* **34**(3) (2015)
9. Zhou, Q.Y., Neumann, U.: 2.5d building modeling by discovering global regularities. In: *CVPR*. (2012)
10. Haene, C., Zach, C., Cohen, A., Angst, R., Pollefeys, M.: Joint 3D scene reconstruction and class segmentation. In: *CVPR*. (2013)
11. Lin, H., Gao, J., Zhou, Y., Lu, G., Ye, M., Zhang, C., Liu, L., Yang, R.: Semantic decomposition and reconstruction of residential scenes from lidar data. *ACM Transactions on Graphics* **32**(4) (2013)
12. Cabezas, R., Straub, J., Fisher, J.: Semantically-aware aerial reconstruction from multi-modal data. In: *ICCV*. (2015)
13. Scharstein, D., Szeliski, R.: A taxonomy and evaluation of dense two-frame stereo correspondence algorithms. *IJCV* **47**(1-3) (2002)
14. Hirschmuller, H.: Stereo processing by semiglobal matching and mutual information. *PAMI* **30**(2) (2008)
15. Zitnick, C., Kang, S.: Stereo for image-based rendering using image over-segmentation. *IJCV* **75**(1) (2007)
16. Taguchi, Y., Wilburn, B., Zitnick, C.: Stereo reconstruction with mixed pixels using adaptive over-segmentation. In: *CVPR*. (2008)
17. Bodis-Szomoru, A., Riemenschneider, H., Van Gool, L.: Fast, approximate piecewise-planar modeling based on sparse structure-from-motion and superpixels. In: *CVPR*. (2014)
18. Bleyer, M., Rother, C., Kohli, P., Scharstein, D., Sinha, S.: Object stereo - joint stereo matching and object segmentation. In: *CVPR*. (2011)
19. Ladicky, L., Sturgess, P., Russell, C., Sengupta, S., Bastanlar, Y., Clocksin, W., Torr, P.: Joint optimization for object class segmentation and dense stereo reconstruction. *IJCV* **100**(2) (2012)
20. Bay, H., Ferrari, V., Van Gool, L.: Wide-baseline stereo matching with line segments. In: *CVPR*. (2005)
21. Zhang, Z., Fidler, S., Waggoner, J., Cao, Y., Dickinson, S., Siskind, J., Wang, S.: Superedge grouping for object localization by combining appearance and shape information. In: *CVPR*. (2012)
22. Sun, X., Christoudias, M., Fua, P.: Free-shape polygonal object localization. In: *ECCV*. (2014)



23. Levinshtein, A., Sminchisescu, C., Dickinson, S.: Optimal contour closure by superpixel grouping. In: ECCV. (2010)
24. Gueguen, L., Hamid, R.: Large-scale damage detection using satellite imagery. In: CVPR. (2015)
25. Zheng, E., Wang, K., Dunn, E., Frahm, J.M.: Minimal solvers for 3d geometry from satellite imagery. In: ICCV. (2015)
26. Groger, G., Plumer, L.: Citygml interoperable semantic 3d city models. *Journal of Photogrammetry and Remote Sensing* **71** (2012)
27. Duan, L., Lafarge, F.: Image partitioning into convex polygons. In: CVPR. (2015)
28. Briese, C., Pfeifer, N., Dorninger, P.: Applications of the robust interpolation for dtm determination. In: *Photogrammetric Computer Vision*. (2002)
29. Hartley, R., Saxena, T.: The cubic rational polynomial camera model. In: *Image Understanding Workshop*. Volume 649. (1997)
30. Boykov, Y., Kolmogorov, V.: An experimental comparison of min-cut/max-flow algorithms for energy minimization in vision. *PAMI* **26**(9) (2004)
31. CGAL. Computational Geometry Algorithms Library. <http://www.cgal.org/>
32. GDAL. Geospatial Data Abstraction Library. <http://www.gdal.org/>
33. Salinas, D., Lafarge, F., Alliez, P.: Structure-Aware Mesh Decimation. *Computer Graphics Forum* **34**(6) (2015)